Chemical Engineering Journal 507 (2025) 160634

Contents lists available at ScienceDirect

Chemical Engineering Journal

journal homepage: www.elsevier.com/locate/cej

Electron delocalization engineering via hierarchical modulation in single-atom catalysts for highly efficient electrochemical CO_2 reduction

Xu Han [a,b], Hong Liu [c,*], Pengfei Cao [d], Weiqiang Tang [e], Chao Yue Zhang [b], Martí Biset-Peiró [b], Ke Xiao [b], Pengyi Tang [c], Marc Heggen [d], Miquel Vega-Paredes [f], Alba Garzón Manjón [a], Lirong Zheng [g,*], Rafal E. Dunin-Borkowski [d], Andreu Cabot [b,h], Kim Daasbjerg [i,j], Joan Ramon Morante [b,k], Ting Zhang [a,b,*], Jordi Arbiol [a,h,*]

[a] Catalan Institute of Nanoscience and Nanotechnology (ICN2), CSIC and BIST, Campus UAB, Bellaterra, Barcelona 08193 Catalonia, Spain
[b] Catalonia Institute for Energy Research (IREC), Jardins de les Dones de Negre 1, Sant Adrià del Besòs, Barcelona 08930 Catalonia, Spain
[c] State Key Laboratory of Information Functional Materials, 2020 X-Lab, Shanghai Institute of Microsystem and Information Technology, Chinese Academy of Sciences, Shanghai 200050, China
[d] Ernst Ruska-Centre for Microscopy and Spectroscopy with Electrons, Forschungszentrum Jülich GmbH, Jülich 52425, Germany
[e] State Key Laboratory of Chemical Engineering and School of Chemical Engineering, East China University of Science and Technology, 200237 Shanghai, China
[f] Max-Planck-Institutfur Eisenforschung GmbH (MPIE), 40237 Dusseldorf, Germany
[g] Beijing Synchrotron Radiation Facility, Institute of High Energy Physics, Chinese Academy of Sciences, Beijing 100049, China
[h] ICREA, Pg. Lluís Companys 23, Barcelona 08010 Catalonia, Spain
[i] Department of Chemistry/Interdisciplinary Nanoscience Center (iNANO) Aarhus University Langelandsgade 140, 8000 Aarhus C, Denmark
[j] Novo Nordisk Foundation (NNF) CO_2 Research Center (CORC), Aarhus University, Gustav Wieds Vej 10C, 8000 Aarhus C, Denmark
[k] Department of Physics, Universitat de Barcelona, Barcelona 08028 Catalonia, Spain

ARTICLE INFO

Keywords:
Single atom catalysts
Electron tug effect
CO_2 electroreduction
High CO selectivity
Wide potential range
Au nanoclusters

ABSTRACT

Modulating the coordination of atomically dispersed MN_4 moieties to enhance electron asymmetry presents a promising strategy for improving catalytic performance in the electrochemical reduction of carbon dioxide (eCO_2RR). By combining small amounts of Au nanoclusters with lateral oxygen coordination in the first coordination shell, the enhanced electron delocalization on Ni centers improves both activity and selectivity. Experimentally, the optimized catalyst demonstrates exceptional catalytic performance, achieving over 95% Faradaic efficiency (FE) for CO across a broad potential range from − 0.50 to − 0.85 V vs. RHE. It also achieves over 90% FE for CO at an overpotential of 340 mV, outperforming state-of-the-art Ni-based single-atom catalysts (SACs). Moreover, the catalyst shows promising potential at a higher current density (~150 mA cm^{-2}) in a flow cell, maintaining high CO selectivity (over 90%). Structural characterizations and theoretical calculations indicate that this structure enhances electron redistribution around Ni sites through a unique electron tug effect. This effectively stabilizes *COOH intermediates, favoring CO production during eCO_2RR at low applied potentials. This work offers a valuable method that extends beyond the first coordination shell, augmenting the complexity of electronic distribution on metal centers, which could be adapted for further fine-tuning the catalytic behavior of SACs in various reactions.

1. Introduction

Highly efficient catalysts for the electrochemical reduction of carbon dioxide (eCO_2RR) are pivotal for achieving a carbon–neutral energy cycle [1,2]. Recently, *d*-block single-atom catalysts (SACs) anchored on carbon-based substrates with a prototypically metal-1st shell coordinated nitrogen (N) atoms MN_4 moiety, have demonstrated significant potential for eCO_2RR [3–5]. The adsorption strength of intermediates on MN_4 during eCO_2RR is generally influenced by the electronic structure of the metal centers [6–8]. Inspired by this, the rational tailor of metal centers in conjunction with the first coordination shell presents a powerful method for enhancing the catalytic performance of SACs. For instance, substituting N atoms with other non-metallic elements (e.g., O [9,10], S [11,12], P [13,14]) in the first coordination shell can facilitate

* Corresponding authors.
E-mail addresses: liuhong01@mail.sim.ac.cn (H. Liu), zhenglr@ihep.ac.cn (L. Zheng), tingzhang@chem.au.dk (T. Zhang), arbiol@icrea.cat (J. Arbiol).

https://doi.org/10.1016/j.cej.2025.160634
Received 21 December 2024; Received in revised form 10 February 2025; Accepted 12 February 2025
Available online 13 February 2025

electron redistribution at the metal centers. This substitution increases the entropy of pristine MN_4, induced by heightened electron disorder at the metal centers, which benefits the catalytic performance of active sites by modulating the adsorption energies of reactants and intermediates [15,16]. To further enhance the complexity of the electronic structure, a strategy combining near-range heteroatom substitution with long-range modulation in the second coordination shell has been proposed [17–20]. This approach intensifies the distortion of the electronic configurations of the *d* orbitals, as the doped heteroatoms in the second shell modulate the local environment of active sites over extended distances. Such modulation can significantly alter the binding energies of critical eCO_2RR intermediates (e.g., *COOH and *CO), thereby improving both selectivity and catalytic activity for eCO_2RR [18–22]. However, the complexities involved in implementing long-range coordination to precisely dope heteroatoms in the second shell significantly limit the widespread adoption of this strategy. Therefore, developing alternative approaches to enhance electron delocalization at the metal center is highly desirable.

In this work, we propose an electron tug effect to refine electron delocalization chaos at atomic Ni sites to enhance eCO_2RR. This is achieved by combining planar coordination of oxygen (O) in the first shell with nearby gold (Au) nanoclusters at various hierarchical scales. Due to the differing electronegativity of O atoms, the engineered NiN_3O sites—where a nitrogen atom is substituted with an oxygen atom in the first shell—can effectively disrupt the electronic and structural symmetry of NiN_4 sites and alter the charge density of Ni centers. Moreover, the spatial and functional compatibility of nanoclusters allows the incorporation of Au clusters as neighbors, which reinforces electron delocalization around NiN_3O sites, resulting in an electron tug effect at the Ni centers. This integration of heteroatoms and nanoclusters

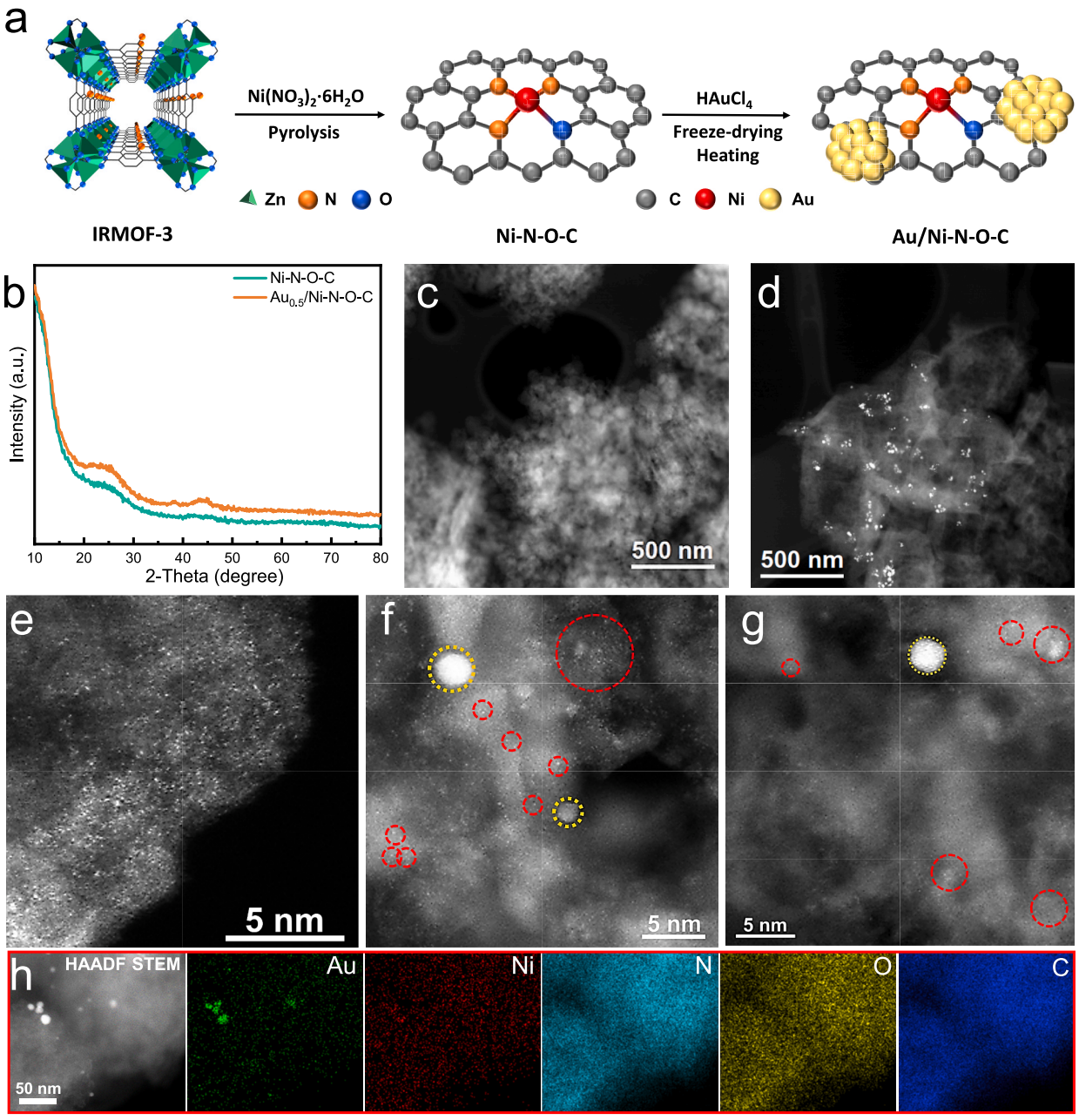

Fig. 1. Synthesis and characterization of catalysts. (a) Schematic illustration of the synthetic process. (b) XRD pattern of Ni-N-O-C and $Au_{0.5}$/Ni-N-O-C, low magnification images of (c) Ni-N-O-C and (d) $Au_{0.5}$/Ni-N-O-C. High magnification AC HAADF-STEM image of (e) Ni-N-O-C and (f-g) $Au_{0.5}$/Ni-N-O-C. (h) HAADF-STEM image and representative EDS chemical composition maps of $Au_{0.5}$/Ni-N-O-C.

significantly alters the electron distribution of Ni centers, enhancing both activity and selectivity. By carefully controlling the amount of Au additive in the unique Ni SAC (NiN_3O), the optimized $Au_{0.5}$/Ni-N-O-C sample demonstrated remarkable eCO_2RR performance, maintaining over 95% Faradaic efficiency for CO (FE_{CO}) across a wide potential range from -0.50 to -0.85 V vs. RHE (notably, 93% at an overpotential of 340 mV) in an H-cell. Additionally, the flow cell assembled with $Au_{0.5}$/Ni-N-O-C sample achieved a current density of $-$ 150 mA/cm^2 with a $FE_{CO} >$ 90%, indicating promising prospects for industrial application. *In-situ* attenuated total reflection infrared (ATR-IR) spectroscopy and theoretical calculations suggest that the decoration of Au clusters on NiN_3O effectively reduces the free energy for *COOH intermediate formation on Ni sites, as the *d*-band center of Ni in Au/Ni-N-O-C is closer to the Fermi level. This paradigm offers an effective strategy to address the challenges associated with precisely modulating the electronic structure of single atoms beyond the first coordination shell.

2. Results and discussion

2.1. Synthesis and characterizations of different catalysts

The Au/Ni-N-O-C was synthesized following the procedure outlined in Fig. 1**a**. Initially, a Ni-doped isoreticular metal–organic framework-3 (IRMOF-3) as a precursor for constructing Ni-O and Ni-N coordination was prepared by a two-step method, leveraging a pore confinement effect. This prepared Ni-doped IRMOF-3 retained the original crystallinity, functional groups, and morphology of IRMOF-3, as confirmed through X-ray diffraction patterns (XRD), Fourier-transform infrared (FTIR) and field emission scanning electron microscope (FE-SEM) analyses (**Figs. S1-S3**). Subsequently, the Ni-N-O-C catalyst was obtained via simple pyrolysis under an Ar atmosphere, which then acted as a substrate for the growth of Au precursors. For comparison, an N-O-C catalyst was produced without Ni single atoms using a similar pyrolysis method. By introducing Au precursors with different concentrations, the Au_x/Ni-N-O-C (x = 0.25, 0.50 or 0.75) catalysts were generated through low-temperature pyrolysis under an Ar atmosphere. The proportion of Ni and Au loading in Ni-N-O-C and $Au_{0.5}$/Ni-N-O-C samples was determined through inductively coupled plasma optical emission spectrometry (ICP-OES) and is detailed in **Table S1**. Additionally, $Au_{0.5}$/N-O-C catalyst was fabricated using N-O-C as the substrate via a similar method.

Following pyrolysis, the crystal structures of N-O-C and Ni-N-O-C substrates were analyzed using XRD (**Fig. S4** and Fig. 1**b**). Notably, these samples displayed distinct similarities in their diffraction patterns, exhibiting two broad peaks around 24° and 44°. These peaks corresponded to the (002) and (100) diffraction planes for graphitic carbon [23,24], indicating the presence of a carbon matrix in the samples after pyrolysis. Moreover, the characteristic peaks associated with metal hybrids were notably absent in the XRD patterns of N-O-C and Ni-N-O-C, supporting that no metal crystalline species formed before the decoration with Au. Raman spectra of N-O-C and Ni-N-O-C samples, as presented in **Fig. S5**, exhibited primary peaks at approximately 1365 and 1590 cm^{-1}, corresponding to the typical defect (D) and graphite (G) bands of graphitic carbon. The I_D/I_G band intensity ratio (1.1) in both samples was consistent, indicating a similar number of defects in both structures [25,26]. The presence of rich structural defects stemmed from vaporized ZnO_4 clusters [9,27]. In the cases of the Au_x/Ni-N-O-C samples, a small new diffraction peak corresponding to the Au (111) plane was observed [28], indicating the successful introduction of Au particles into the N-O-C or Ni-N-O-C substrates (Fig. 1**b** and **Fig. S6**). Meanwhile, the XRD patterns (**Fig. S6**) demonstrated an increase in the yield of crystalline Au particles with the elevated concentration of the Au precursor in Au_x/Ni-N-O-C.

The morphology, structure, and elemental distribution of samples were characterized using aberration corrected (AC) high angle annular dark field (HAADF) scanning transmission electron microscopy (STEM). The low-magnification HAADF-STEM images shown in Fig. 1**c-d** and **Fig. S7** demonstrate that all samples transformed into sheet-like morphology, indicating that the pyrolysis process alters the original structure of the MOF precursors. Notably, the absence of bright nanoparticles/clusters in N-O-C and Ni-N-O-C samples suggests no Ni nanoparticle or cluster formation after pyrolysis, aligning with the XRD results. Compared with the low-magnification HAADF STEM images of N-O-C and Ni-N-O-C, small bright dots were observed on $Au_{0.5}$/Ni-N-O-C shown in Fig. 1**d** at the same magnification, revealing the successful introduction of Au nanoclusters on the $Au_{0.5}$/Ni-N-O-C catalyst. The different Z contrast among Ni, N, O, and C elements allowed for the clear identification of homogeneously distributed Ni single sites (encircled by red dotted lines) in the local AC HAADF STEM images of Ni-N-O-C (Fig. 1**e** and **Figs. S8**) and $Au_{0.5}$/Ni-N-O-C (Fig. 1**f-g** and **Fig. S9**), supporting the successful anchoring of Ni single atoms in both samples. Furthermore, Fig. 1**f-g** and **Fig. S9** confirm the presence of some Au nanoclusters (encircled by yellow dotted line). It is worth noting that multiple areas of the $Au_{0.5}$/Ni-N-O-C sample were examined and only a few Au nanoparticles showed good crystallinity due to their large particle size. A more in-depth examination of the large Au nanoparticles displays well-defined lattice fringes of Au (1 1 1) and Au (002) planes (**Fig. S10**). Energy dispersive X-ray spectroscopy (EDS) mapping results for $Au_{0.5}$/Ni-N-O-C and Ni-N-O-C samples are illustrated in Fig. 1**h** and **Fig. S11**. These mappings not only reveal the uniform distribution of Ni, N and O dispersed throughout the carbon matrix but also clearly identify the presence of Au nanoclusters, encircled by Ni species. In addition, EDS mapping results of $Au_{0.5}$/N-O-C show obvious Au signals on N-O-C substrate (**Fig. S12**).

X-ray photoelectron spectroscopy (XPS) analysis has been used to identify the potential bonding structure and local chemical configuration of N-O-C, Ni-N-O-C and $Au_{0.5}$/Ni-N-O-C. When compared to the N-O-C sample without the introduction of Ni single atoms, a distinctive peak at 530.5 eV appears in the high-resolution O 1s spectroscopy of Ni-N-O-C and $Au_{0.5}$/Ni-N-O-C. This peak is attributed to Ni-O bond, potentially suggesting the retention of Ni-O chelation post-calcination (Fig. 2**a** and **Fig. S13**). Notably, a porphyrin-like moiety at 399.7 eV, corresponding to the Ni-N coordination, can be observed in both Ni-N-O-C and $Au_{0.5}$/Ni-N-O-C, supporting the presence of atomically dispersed Ni sites in both samples (Fig. 2**b** and **Fig. S14**) [29,30]. These findings strongly suggest that the isolated Ni atoms are coordinated with N and O atoms in Ni-N-O-C and $Au_{0.5}$/Ni-N-O-C samples. This observation could be further confirmed by the X-ray absorption spectroscopy (XAS). The C 1s XPS spectra for all samples, as displayed in **Fig. S15**, reveal four distinct peaks at binding energies of 284.5, 285.4, 286.2 and 287.3 eV. These correspond to graphitic sp^2 carbon (C=C), C-C, carbon coordinated with doped O and N (C-N and C-O), and C=O bonds, respectively, indicating a common origin of these samples from the same MOFs precursors [31,32]. Due to the low content, there is no obvious peak in Ni 2p XPS spectra for both samples (**Fig. S16**). In Fig. 2**c** and **Fig. S17**, a spin–orbit doublet for Au 4f at 84.0 eV and 87.7 eV is evident, signifying that Au was successfully introduced onto the Ni-N-O-C/N-O-C substrate after the low-temperature pyrolysis [33].

Furthermore, XAS were conducted at the Ni K-edge for Ni-N-O-C, $Au_{0.5}$/Ni-N-O-C, and different reference samples to confirm the local coordination structure and valence of the atomically dispersed Ni. The X-ray absorption near edge structure (XANES) K-edge spectra of nickel phthalocyanine (NiPc), Ni-N-O-C, and $Au_{0.5}$/Ni-N-O-C exhibit similar characteristic features, which fall between those of metallic Ni foil and NiO reference, suggesting that the valence state of the Ni in NiPc, Ni-N-O-C and $Au_{0.5}$/Ni-N-O-C ranges between 0 and + 2 (Fig. 2**d**) [34,35]. In the inset of Fig. 2**d**, the pre-edge feature peak at approximately 8330 eV is assigned to the 1s → 3d transition of the central Ni atoms. This transition is typically forbidden in centrosymmetric point groups [36]. In comparison to the weak peak observed in planar complexes NiPc, exhibiting a high D_{4h} centrosymmetry, there is an increase in peak intensity observed in Ni-N-O-C and $Au_{0.5}$/Ni-N-O-C, which is due to *p*-

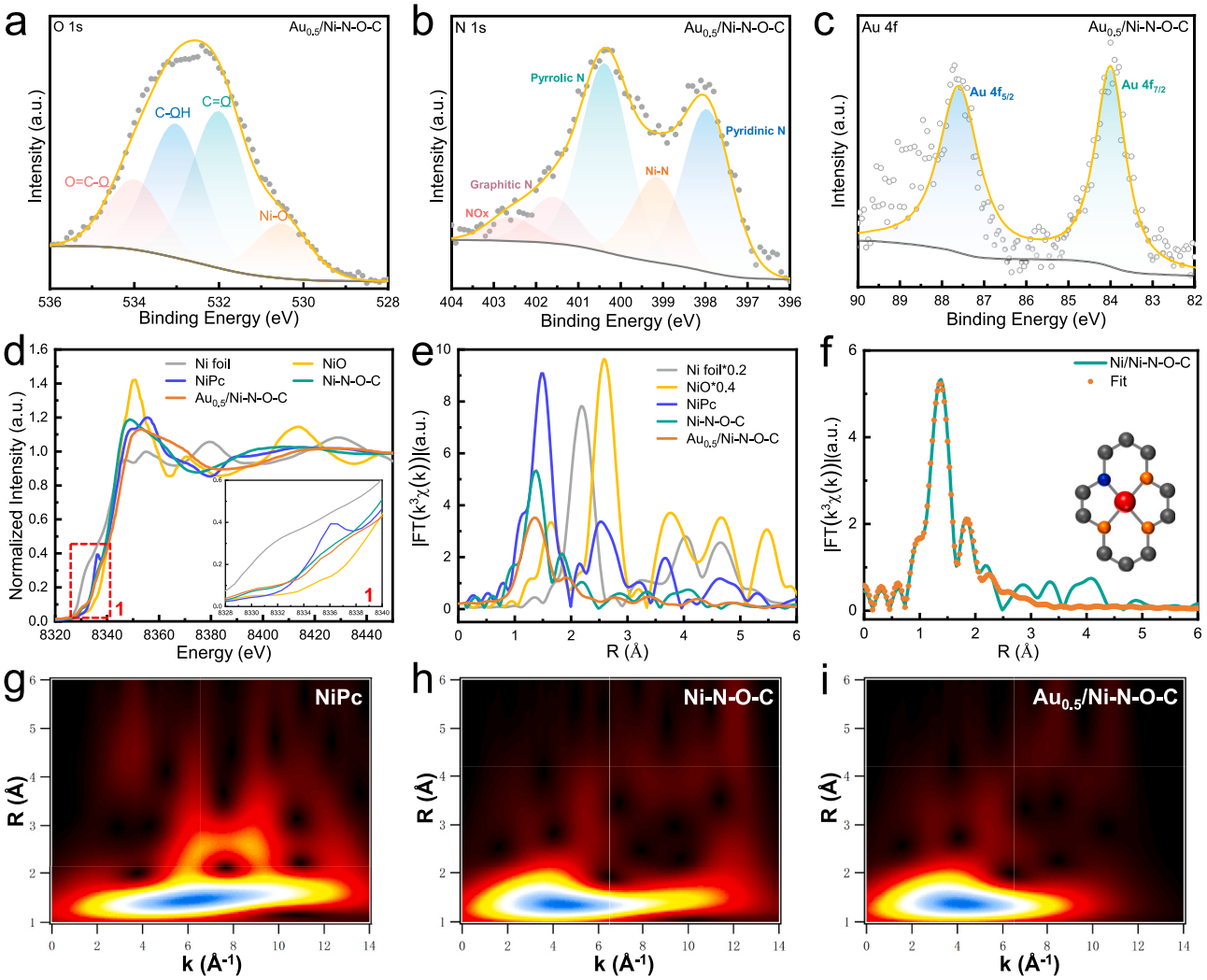

Fig. 2. Electronic structure characterization of catalysts. High-resolution XPS of (a) O 1 s, (b) N 1 s and (c) Au 4f spectrum of $Au_{0.5}$/Ni-N-O-C. (d) XANES spectra of the Ni-N-O-C and $Au_{0.5}$/Ni-N-O-C at Ni K-edge. The insets in (d) are the magnified corresponding regions. (e) EXAFS spectra at Ni K-edge on Ni-N-O-C and $Au_{0.5}$/Ni-N-O-C. (f) The corresponding Ni K-edge EXAFS fitting parameters for Ni-N-O-C sample. (Ni, O, N, C atoms are represented in red, blue, orange, and grey, respectively). WT-EXAFS of (g) NiPc, (h) Ni-N-O-C and (i) $Au_{0.5}$/Ni-N-O-C. (For interpretation of the references to colour in this figure legend, the reader is referred to the web version of this article.)

d mixing in non-centrosymmetric geometries [36–38]. Regarding the 1s → $4p_z$ transition near 8336 eV, NiPc showed a distinct transition characteristic of square-planar MN_4 moieties. However, the intensity of this transition in Ni-N-O-C and $Au_{0.5}$/Ni-N-O-C is weaker because of the distorted D_{4h} symmetry of the Ni atom [13,39,40]. The D_{4h} symmetry in Ni-N-O-C and $Au_{0.5}$/Ni-N-O-C is distorted due to the replaced oxygen in the lateral coordination. Meanwhile, a noticeable decrease in intensity is observed in $Au_{0.5}$/Ni-N-O-C compared to Ni-N-O-C, suggesting a higher distortion of isolated Ni atoms in $Au_{0.5}$/Ni-N-O-C due to the electron tug effect caused by the augmentation of O and Au nanoclusters (inset of Fig. 2**d**). Meanwhile, a shift to high energy area of XANES K-edge spectra on $Au_{0.5}$/Ni-N-O-C was observed in comparison to Ni-N-O-C, suggesting that the higher valence state of Ni in $Au_{0.5}$/Ni-N-O-C. The Fourier transform (FT) k^2-weighted $\chi(k)$ functions of the Ni K-edge EXAFS of different samples are displayed in Fig. 2**e**. All samples exhibit a primary peak at approximately 1–2 Å, attributed to the first metal–metal/N/O shell. The first Ni-N/O coordination shell at 1.40 Å in Ni-N-O-C and $Au_{0.5}$/Ni-N-O-C catalysts differs significantly from Ni foil (Ni-Ni path at 2.1 Å) and NiO (Ni-O path at 1.60 Å [41,42]. Additionally, the absence of metallic Ni-Ni scattering supports the atomically dispersed nature of single Ni sites in prepared Ni-N-O-C and $Au_{0.5}$/Ni-N-O-C catalysts [42]. Compared to NiPc, the peak positions slightly shift leftward on Ni-N-O-C and $Au_{0.5}$/Ni-N-O-C, indicating a change in the coordination configuration of mixed Ni-N and Ni-O forms [22,43]. To further elucidate the detailed atomic structure of Ni-N-O-C, quantitative extend X-ray adsorption fine structure (EXAFS) analyses were performed, and the fitting results are shown in Fig. 2**f**. Based on the fitting outcomes and the corresponding parameters listed in **Table S2**, the coordination number of the Ni-N-O-C catalyst is determined to be 4 (comprising three bond lengths of 1.87 Å for Ni-N and one bond length of 2.12 Å for Ni-O). More information about the radial distance k-space resolution was obtained by wavelet transform (WT) EXAFS analysis (Fig. 2**g-2i** and **Fig. S18**). The WT contour at ≈4 $Å^{-1}$ for Ni-N-O-C and $Au_{0.5}$/Ni-N-O-C is close to NiO and moving toward NiPc, indicating the presence of atomically dispersed Ni-N sites and Ni-O coordination [44]. Therefore, the spectra obtained on the Ni-N-O-C sample are fitted assuming the presence of $Ni_1N_3O_1$ sites, consistent with the preceding analyses, which is expected to bring desirable catalytic performance.

2.2. *Electrochemical CO_2-to-CO performance evaluation*

The catalysts' electrochemical performances for CO_2 reduction were evaluated in a CO_2-saturated 0.5 M $KHCO_3$ solution using a standard three-electrode H-cell. To initially assess the eCO_2RR, linear sweep

voltammetry (LSV) curves were conducted for all samples. Fig. S19 and Fig. 3**a** illustrate an increased current density in CO_2-saturated solutions compared to those in Ar-saturated electrolytes, confirming the electrochemical reduction of CO_2 on N-O-C, Ni-N-O-C, $Au_{0.5}$/N-O-C and $Au_{0.5}$/Ni-N-O-C samples [45,46]. Moreover, in comparison to N-O-C and $Au_{0.5}$/N-O-C, both Ni-N-O-C and $Au_{0.5}$/Ni-N-O-C exhibited increased current density within the measured potential range, highlighting the significant role of the single Ni active sites in eCO_2RR. Notably, it is important to mention that $Au_{0.5}$/Ni-N-O-C displayed the smallest onset potential among the four catalysts, indicating a higher eCO_2RR catalytic activity. Gas products were regularly analyzed via online gas chromatography (GC), revealing that CO and H_2 were the primary gases obtained across all samples. Additionally, the liquid-phase products of $Au_{0.5}$/Ni-N-O-C were examined using nuclear magnetic resonance (^1H NMR) spectroscopy after the electrochemical CO_2 reduction processes. These analyses demonstrated the absence of any liquid products (Fig. S20). Subsequently, potentiostatic electrolysis of CO_2 at different potentials was employed to further scrutinize the catalytic performances within a range from -0.40 to -0.95 V vs. RHE. The total current density measured for N-O-C, Ni-N-O-C, $Au_{0.5}$/N-O-C and $Au_{0.5}$/Ni-N-O-C samples is summarized in Fig. S21. Under the same catalyst mass loading (approximately 1 mg cm^{-2}), the $Au_{0.5}$/Ni-N-O-C demonstrated the highest current density on each applied potential compared to N-O-C, $Au_{0.5}$/N-O-C, and Ni-N-O-C catalysts. This suggests that the enhanced activity of $Au_{0.5}$/Ni-N-O-C is mainly attributed to the electron tug effect of lateral O substitution and Au nanoclusters. The Faradaic efficiency (FE) for CO production was assessed within the potential range from -0.40 to -0.95 V (vs. RHE) for all synthesized catalysts, as shown in Fig. 3**b** and Fig. S22**a**. The increased FE of CO on Ni-N-O-C compared to N-O-C suggests the crucial role of Ni single atoms in eCO_2RR. Typically, for most single-atom catalysts reported, the FE_{CO} tends to decline rapidly after the optimal potential. Interestingly, $Au_{0.5}$/Ni-N-O-C catalyst showed continuous maintenance of high FE_{CO} (95%) under a broad potential range (-0.50 to -0.85 V vs. RHE), outperforming Ni-N-O-C, $Au_{0.5}$/N-O-C, and N-O-C throughout the potential window. Additionally, when compared to previously reported Ni-based SACs or Au-based electrocatalysts (Fig. S32 and Table S3), the $Au_{0.5}$/Ni-N-O-C electrocatalyst exhibited a lower overpotential (340 mV) to achieve $FE_{CO} >$ 90% and a broader potential window with FE_{CO} surpassing 95%. This supports the notion that the electron tug effect plays a pivotal role in

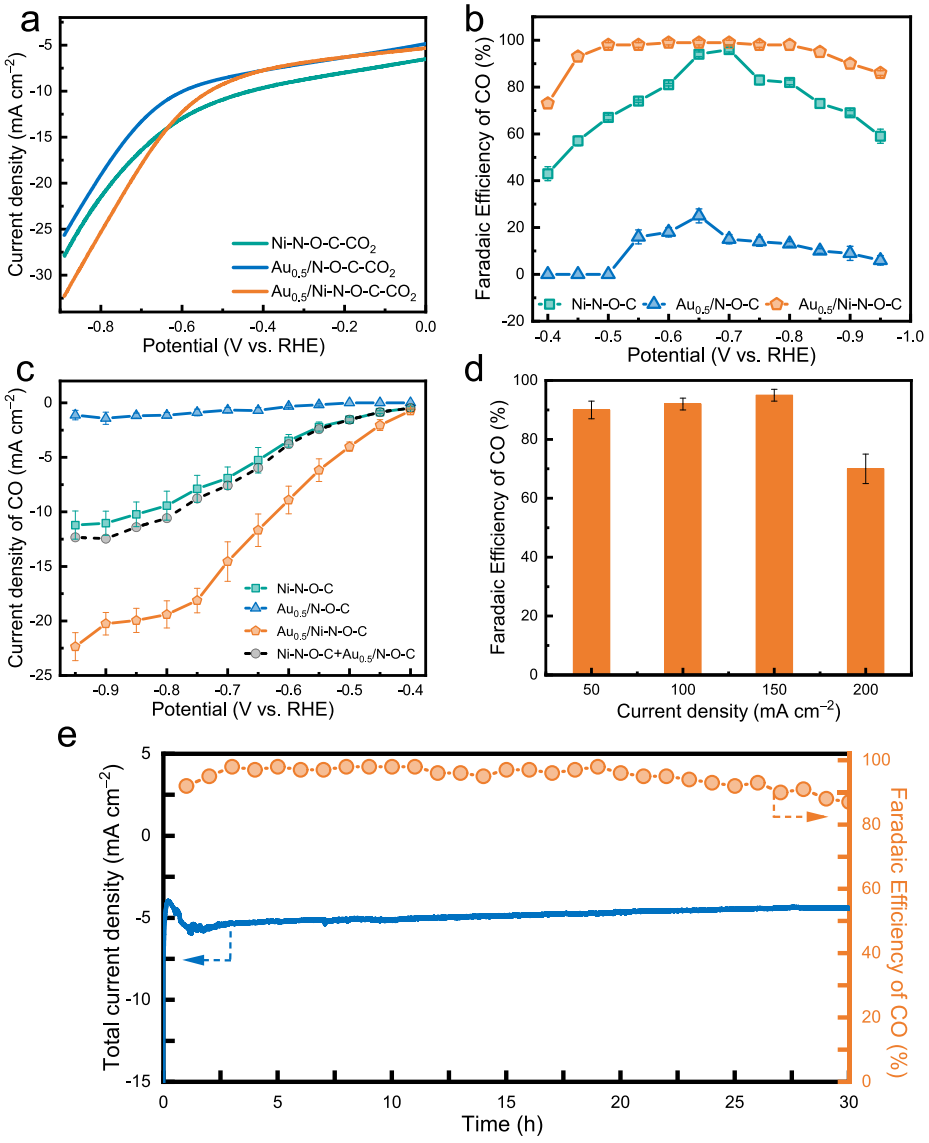

Fig. 3. Electrochemical CO_2RR Performances. (a) LSV curves. (b) Faradaic efficiencies of CO. (c) Current density for CO production. (d) FE_{CO} on the $Au_{0.5}$/Ni-N-O-C catalyst in the range of current densities from 50 to 200 mA cm^{-2} in a flow cell configuration with 1.0 M $KHCO_3$ as electrolyte. (e) Stability test of $Au_{0.5}$/Ni-N-O-C at -0.50 V vs. RHE.

enhancing eCO_2RR and overcoming limitations in improving eCO_2RR performance on Ni-based SACs. The turnover frequency (TOF) of CO production for Ni-N-O-C and $Au_{0.5}$/Ni-N-O-C was calculated based on the current density of eCO_2RR and the FE of CO. A larger TOF on $Au_{0.5}$/Ni-N-O-C (4000 h^{-1}) confirmed an intrinsically higher eCO_2RR activity in comparison of Ni-N-O-C. The above analysis showed that the kinetics for Ni-N-O-C have been improved by the introduction of Au nanoclusters via the electron tug effect (**Fig. S23**). The CO current density of the $Au_{0.5}$/Ni-N-O-C catalyst surpassed that of Ni-N-O-C and $Au_{0.5}$/N-O-C on each applied potential (Fig. 3**c**), and even exceeded their combined value (dash line). This revelation suggests that the improved CO selectivity of $Au_{0.5}$/Ni-N-O-C is not merely a result of the composite effect of Ni single atoms and Au nanoclusters but is primarily attributed to the novel effect induced by the presence of Au nanoclusters and the Ni single sites. This observation is further corroborated by the catalytic performance obtained from the $Au_{0.5}$/Ni-N-O-C-physical mixture sample (**Fig. S24**). In contrast to the $Au_{0.5}$/Ni-N-O-C, the $Au_{0.5}$/Ni-N-O-C-physical mixture sample displayed a decreased FE_{CO} at all applied potentials. However, it still exhibited a similar trend in FE_{CO}, which further demonstrates the interplay formed between Au nanoclusters and Ni SACs. As the potential shifted towards a more negative value, the FE(CO) s for Ni-N-O-C, $Au_{0.5}$/N-O-C and N-O-C gradually decreased since the competitive hydrogen evolution reaction (HER) became the dominant reaction, evident in the FE (H_2) shown in **Fig. S25a** and **Fig. S22a**. However, the FE(CO) of $Au_{0.5}$/Ni-N-O-C decreased negligibly as the potential became more negative. When potential reached − 0.95 V vs. RHE, the FE (CO) still maintained 86%. The potential-dependent H_2 current densities for the different catalysts are illustrated in **Fig. S22b** and **Fig. S25b**. These comparisons further demonstrate that electron tug effect in $Au_{0.5}$/Ni-N-O-C achieving electron redistribution around active sites can significantly enhance both high catalytic activity and selectivity to produce CO over a broad potential range. Notably, the $Au_{0.5}$/Ni-N-O-C catalyst demonstrated remarkable stability, maintaining nearly unchanged current density values and an FE_{CO} of over 85% after 30 h of electrolysis at -0.50 V vs. RHE (Fig. 3**e**). As shown in **Fig. S26**, XRD and XPS measurements were performed on $Au_{0.5}$/Ni-N-O-C coated on the carbon paper (CP) both before and after the electrocatalysis. No noticeable difference in the crystal structure was observed in XRD patterns after the electrocatalysis test in 0.5 M $KHCO_3$. However, compared to the fresh sample, there is an obvious difference in high-resolution XPS Ni 2p spectra of $Au_{0.5}$/Ni-N-O-C, which indicates that the Ni singe atoms gradually changed along with long-term electrocatalysis. To further reveal the viability of the $Au_{0.5}$/Ni-N-O-C catalyst, we examined its performance in a gas diffusion electrode (GDE)-based flow cell. This configuration aimed to achieve highly effective CO_2-to-CO conversion over the $Au_{0.5}$/Ni-N-O-C catalyst at industrial current density by mitigating the mass transport limitation of CO_2 gas [47]. The $Au_{0.5}$/Ni-N-O-C catalyzed eCO_2RR in the flow cell could maintain more than 90% FE_{CO} values under a range of current densities from 50 to 150 mA cm^{-2}, indicating the promising applicability of $Au_{0.5}$/Ni-N-O-C for industrial eCO_2RR (Fig. 3**d**). These results demonstrate the industrial superiority and practicality of this catalyst. However, it is important to note that at a current density of 200 mA cm^{-2}, the FE of CO significantly dropped due to the unavoidable flooding of carbon paper-based GDEs or the catalyst's destruction under high current density.

To elucidate the reason behind the enhanced catalytic performance of $Au_{0.5}$/Ni-N-O-C, we initially excluded the contribution of electrochemical surface area (ECSA) derived from double layer capacitance (C_{dl}), as summarized in **Fig. S27a-e**. The slope in these graphs could serve as a reference for ECSA. Ni-N-O-C displayed the same C_{dl} (28 mF cm^{-2}) as N-O-C (28 mF cm^{-2}) but exhibited higher selectivity, indicating that the isolated Ni single metal active sites in Ni-N-O-C are the primary catalytic sites. This comparison revealed that introducing atomically dispersed metal sites into the N-O-C substrate significantly enhanced the activity of eCO_2RR [23,48]. However, both $Au_{0.5}$/N-O-C and $Au_{0.5}$/Ni-N-O-C samples displayed relatively smaller C_{dl} values (19 mF cm^{-2} and 20 mF cm^{-2}, respectively). This suggests that introducing Au nanoclusters into the catalysts blocked some active sites in the original Ni-N-O-C or N-O-C. Despite this, $Au_{0.5}$/Ni-N-O-C exhibited higher selectivity compared to Ni-N-O-C. This observation implies that the intrinsic catalytic activity of $Au_{0.5}$/Ni-N-O-C does not linearly correlate with high ECSA. More likely, the eCO_2RR catalytic properties of $Au_{0.5}$/Ni-N-O-C arise from the higher intrinsic activity of the Ni active site adjacent to the Au nanoclusters, underscoring the positive influence of Au nanoclusters surrounded by Ni SACs in enhancing eCO_2RR activity. Moreover, Nyquist plots revealed that the $Au_{0.5}$/Ni-N-O-C and Ni-N-O-C samples had lower interfacial charge-transfer resistance (R_{CT}) compared to N-O-C and $Au_{0.5}$/N-O-C (see **Fig. S27f**) [49]. Additionally, various Au_x/Ni-N-O-C catalysts with different Au contents are shown in **Fig. S28**. These results demonstrate that the presence of a specific amount/density of Au nanoclusters indeed influences the generation of CO at different applied potentials. This highlights the importance of optimizing the Au content to achieve a balance where the electron tug effect is enough to achieve a high selectivity and activity towards CO. As a result, to attain the optimal activity of Au/Ni-N-O-C, it is crucial to adjust the quantity of Au reagent to a point where the formed electron tug effect could broad the potential range with high selectivity and activity toward CO.

2.3. Mechanism studies

The *COOH and *CO are important intermediates in the formation of CO during eCO_2RR. To specifically detect absorbed intermediate species and understand the reaction mechanisms, *in-situ* attenuated total reflection surface enhanced infrared absorption spectroscopy (ATR-SEIRAS) was conducted on Ni-N-O-C and $Au_{0.5}$/Ni-N-O-C samples during potential stepwise sweeps from -0.40 V to -0.90 V vs. RHE in a CO_2-saturated 0.5 M $KHCO_3$ solution. Several absorbance bands were observed between 2400 and 1000 cm^{-1} for both samples (Fig. 4**a-b**). Notably, there was no distinct band at 1830 cm^{-1}, which is associated with the vibration feature of bridge-bonded CO (CO_B), throughout the entire potential window. This suggests the presence of atomically dispersed sites as the active sites [50]. Two prominent peaks observed in Fig. 4**a-b** centered at 2350 cm^{-1} and 1650 cm^{-1}, indicate the consumption of CO_2 and adsorbed H_2O in the solution, respectively [39]. Peaks around 1461 and 2100 cm^{-1} can be attributed to the adsorbed *COOH and *CO intermediates, respectively, which are the main reaction intermediates during the eCO_2RR [50–52]. However, the intensities of the *COOH peaks on $Au_{0.5}$/Ni-N-O-C increased significantly at a relatively low applied potentials (from -0.40 V vs. RHE), suggesting that the *COOH intermediate is generated more readily on $Au_{0.5}$/Ni-N-O-C at lower potentials during eCO_2RR. Furthermore, on the $Au_{0.5}$/Ni-N-O-C sample, peaks at 2010 cm^{-1} appeared at potentials as low as -0.40 V vs. RHE and persisted up to -0.90 vs. RHE, indicating rapid protonation of *COOH to form *CO species at low applied potentials (Fig. 4**c**). In contrast, as shown in Fig. 4**d**, the *CO band was only clearly present on the Ni-N-O-C sample at relatively high potential (from -0.70 vs. RHE). These results indicate that the enhanced eCO_2RR on $Au_{0.5}$/Ni-N-O-C is primarily linked to the rapid protonation of *COOH to form *CO species.

Density Functional Theory (DFT) calculations were employed to further investigate the electrocatalytic mechanism underlying the enhanced eCO_2RR performance of the $Au_{0.5}$/Ni-N-O-C sample, attributed to an electron tug effect. Using the characterizations mentioned above, simulation models were developed for both Ni-N-O-C and Au/Ni-N-O-C catalysts. The Ni-N-O-C catalyst was built with a Ni atom coordinated with 3 nitrogen atoms and 1 oxygen atom by replacing six C atoms in a graphene surface. The Au/Ni-N-O-C sample was created by introducing the Au_5 nanocluster around the above single Ni atomic sites (NiN_3O). Additionally, the Au_5 nanocluster was also simulated to represent the prepared Au/N-O-C catalysts. Details on model construction and optimized configurations can be found in Supporting Information and **Fig. S29**. **Fig. S30** illustrates three elemental steps in the

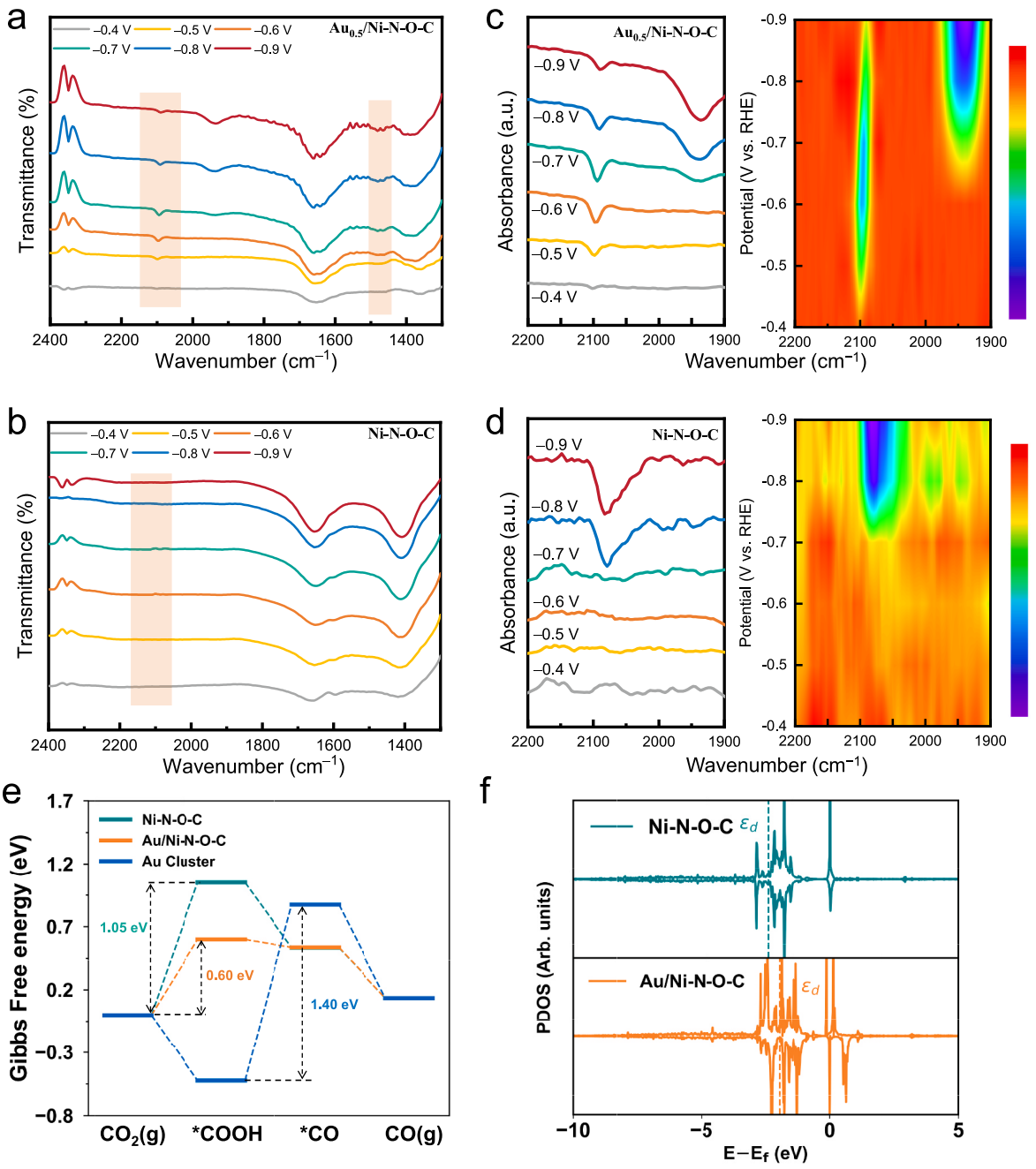

Fig. 4. *In-situ* ATR-IR analysis and DFT calculations. *In-situ* ATR-IR spectra of (a) $Au_{0.5}$/Ni-N-O-C and (b) Ni-N-O-C. High resolution *In-situ* ATR-IR analysis of (c) $Au_{0.5}$/Ni-N-O-C and (d) Ni-N-O-C. (e) Free energy profiles for the eCO_2RR to CO on simulated models. (f) Projected *d*-density of states (PDOS) of Ni over (a) Ni-N-O-C and (b) Au/Ni-N-O-C surfaces.

conversion CO_2-to-CO conversion, involving two proton/electron transfer steps: first, the protonation of a CO_2 molecule to form *COOH ($CO_2 + H^+ + e^- + * \rightarrow$ *COOH); followed by the subsequent conversion of *COOH to *CO and H_2O (*COOH + $H^+ + e^- \rightarrow$ *CO + H_2O) and the desorption of formed *CO from the surface of the active site, where * signifies the adsorption site on the catalyst surface [53]. Clearly, the binding energies of the key intermediates, *COOH formation and *CO desorption, are critical steps during eCO_2RR. As shown in Fig. 4**e**, the free energy profiles of CO_2 reduction to CO on all models were calculated. For both the Ni-N-O-C and Au/Ni-N-O-C models, the formation of *COOH serves as the potential-determining step. The primary distinction between the two models lies in the presence or absence of Au clusters around the Ni center. In the Ni-N-O-C model, the ΔG for the potential-determining step is 1.05 eV, whereas in the Au/Ni-N-O-C model, it is reduced to 0.60 eV. This indicates that the formation of *COOH on highly dispersed Ni sites requires a more negative limiting potential. However, introducing Au nanoclusters around the Ni center lowers the ΔG of this step, promoting the formation of the *COOH intermediate. From a thermodynamic perspective, the synthesized Au/Ni-N-O-C exhibits superior catalytic activity compared to Ni-N-O-C, which aligns with our experimental results. To confirm that the enhanced activity does not originate from the Au clusters themselves, we also calculated the eCO_2RR process on the Au cluster. It was found that, for the Au cluster model, the potential-determining step is the conversion of *COOH to *CO and H_2O, with a ΔG of 1.40 eV, which is higher than the ΔG of the potential-determining steps on Au/Ni-N-O-C models. A similar

phenomenon was observed in the Au(111) model (Fig. S31). Therefore, we hypothesize that the improved activity is not solely due to the Au clusters, but rather due to the interaction between the Au clusters and the Ni center, which enhances the catalytic activity of the Ni center as the active site. To further investigate the difference in activity between the Ni-N-O-C and Au/Ni-N-O-C models, the projected density of states (PDOS) for both models was calculated. The results show that, compared to the Ni-N-O-C model, the *d*-band center of the Au/Ni-N-O-C model is closer to the Fermi level, as shown in Fig. 4**f**. This suggests that the introduction of Au nanoclusters around the Ni site alters the *d*-orbital occupation of the Ni single atom, leading to stronger interactions between the Au/Ni-N-O-C model and *COOH [54].

3. Conclusions

In summary, our study presents a strategy to enhance electronic delocalization around Ni sites through an induced electron-tugging effect, significantly improving the performance of the eCO_2RR. The $Au_{0.5}$/Ni-N-O-C catalysts demonstrated much higher activity compared to NiN_3O alone and most unmodified Ni SACs, achieving a high FE (CO) at low overpotentials and across an exceptionally wide potential range, maintaining over 95% FE_{CO}. DFT calculations indicate that the incorporation of nanoclusters and heteroatoms alters the electronic structure and shifts the *d*-band center of Ni closer to the Fermi level. This adjustment reduces the free energy required for the formation of *COOH on Ni centers, thereby enhancing both CO_2 conversion activity and selectivity. The proposed strategy for SACs with engineered electron redistribution can be extended to explore other advanced electrocatalytic systems.

4. Methods

4.1. Preparation of IRMOF-3

In this procedure, the fabrication process of IRMOF-3 follows the methodology reported in our previous work [25]. Specifically, 932 mg $Zn(NO_3)_2{\cdot}6H_2O$ was dissolved in 100 ml DMF under magnetic stirring at room temperature to create a homogeneous solution. Subsequently, 181 mg 2-aminoterphthalic acid was added to the above mixture and subjected to ultrasonication for several minutes at room temperature until a clear solution formed. The resulting homogeneous solution was then placed in a Teflon-lined stainless-steel autoclave and allowed to react at 100 °C for 24 h. Upon cooling to room temperature, the powder was collected by centrifugation and washed multiple times with DMF and ethanol to eliminate any organic and inorganic residues. The final products were subsequently dried under vacuum at 65 °C for overnight.

4.2. Preparation of Ni-doped IRMOF-3

100 mg IRMOF-3 powder was dispersed in 10 ml of DMF under ultrasound for 10 min at room temperature. After achieving a homogeneous solution, a $Ni(NO_3)_2{\cdot}6H_2O$ aqueous solution (10 mg/ml, 50 μL) was gradually added dropwise into the above solution under ultrasound for 5 min at room temperature. Subsequently, the mixed solution was magnetically stirred at room temperature for 3 h. Following the reaction, the powder was collected through centrifugation, washed multiple times with DMF and ethanol, and dried under vacuum at 65 °C for overnight.

4.3. Preparation of N-O-C and Ni-N-O-C

The as-prepared Ni-doped IRMOF-3 (or IRMOF-3) powders were placed on a porcelain boat. Subsequently, the samples were introduced into a tube furnace and heated at 950 °C for 2 h with a heating rate of 5 °C min^{-1} under an Ar atmosphere to produce dispersed Ni-N-O-C or N-O-C without metal introduction.

4.4. Preparation of Au_x/Ni-N-O-C and Au/N-O-C

To obtain $Au_{0.5}$/Ni-N-O-C and Au/N-O-C, 20 mg Ni-N-O-C or N-O-C was dispersed in 6 mL water and vigorously sonicated for 1 h. Following this, 0.12 mL $HAuCl_4$ solution (1 mg/0.6 mL) was slowly added dropwise into the above suspension under vigorous stirring for 30 min. The adsorbed Au precursor was then rapidly frozen using liquid nitrogen, followed by overnight freeze-drying. The resulting dried powder was heated at 200 °C in a tube furnace under Ar gas flow for 2 h with a heating rate of 5 °C min^{-1}. Adjusting the volume of the Au precursor solution allowed for the creation of $Au_{0.25}$/Ni-N-O-C (0.06 mL) and $Au_{0.75}$/Ni-N-O-C (0.18 mL) using the same process as $Au_{0.5}$/Ni-N-O-C. Additionally, the procedure synthesizing Au/N-O-C was similar to that of $Au_{0.5}$/Ni-N-O-C but using N-O-C as the substrate instead of Ni-N-O-C.

4.5. Preparation of physical mixture $Au_{0.5}$/Ni-N-O-C (labelled as $Au_{0.5}$/Ni-N-O-C-physical mixture)

To prepare the $Au_{0.5}$/Ni-N-O-C-physical mixture sample, the synthesis procedure was the same as that used for $Au_{0.5}$/Ni-N-O-C without the 200°C heating step.

All additional experimental and characterization details are provided in the **supplementary information**, including XRD patterns, FTIR, SEM, TEM, HAADF-STEM, BET, TGA, ICP, Raman spectra, EXAFS, XPS, gas calibration, ^1H NMR, FE (H_2/CO), CV, Tafel slopes, LSV, EIS and the DFT results.

CRediT authorship contribution statement

Xu Han: Writing – review & editing, Writing – original draft, Validation, Methodology, Investigation, Formal analysis, Data curation, Conceptualization. **Hong Liu:** Writing – review & editing, Investigation, Formal analysis. **Pengfei Cao:** Writing – review & editing, Formal analysis, Data curation. **Weiqiang Tang:** Writing – review & editing, Formal analysis, Data curation. **Chao Yue Zhang:** Writing – review & editing, Investigation, Formal analysis. **Martí Biset-Peiró:** Writing – review & editing, Investigation, Formal analysis. **Ke Xiao:** Investigation, Formal analysis. **Pengyi Tang:** Writing – review & editing, Methodology, Investigation, Formal analysis. **Marc Heggen:** Writing – review & editing, Validation, Supervision. **Miquel Vega-Paredes:** Writing – review & editing, Formal analysis. **Alba Garzón Manjón:** Writing – review & editing, Supervision, Formal analysis. **Lirong Zheng:** Writing – review & editing, Formal analysis. **Rafal E. Dunin-Borkowski:** Writing – review & editing, Supervision, Resources. **Andreu Cabot:** Writing – review & editing, Validation, Supervision, Resources, Project administration, Funding acquisition. **Kim Daasbjerg:** Writing – review & editing, Supervision, Resources, Funding acquisition. **Joan Ramon Morante:** Writing – review & editing, Supervision, Resources, Funding acquisition. **Ting Zhang:** Writing – review & editing, Writing – original draft, Visualization, Validation, Supervision, Methodology, Investigation, Funding acquisition, Formal analysis, Data curation, Conceptualization. **Jordi Arbiol:** Writing – review & editing, Writing – original draft, Visualization, Validation, Supervision, Resources, Project administration, Methodology, Funding acquisition, Conceptualization.

Declaration of competing interest

The authors declare the following financial interests/personal relationships which may be considered as potential competing interests: Jordi Arbiol reports financial support was provided by Government of Catalonia. Ting Zhang reports financial support was provided by European Commission. Xu Han reports financial support was provided by European Commission. Weiqiang Tang reports financial support was provided by National Natural Science Foundation of China. Weiqiang Tang reports financial support was provided by Young Elite Scientists Sponsorship Program by CAST. Jordi Arbiol reports financial support

was provided by Horizon Europe. Jordi Arbiol reports financial support was provided by State Agency of Research. If there are other authors, they declare that they have no known competing financial interests or personal relationships that could have appeared to influence the work reported in this paper.

Acknowledgments

The authors thank Guillaume Sauthier, Javier Saiz for the XPS spectrum and FTIR tests at ICN2. ICN2 and IREC acknowledge funding from Generalitat de Catalunya projects 2021SGR00457 and 2021SGR01581, respectively. This study is part of the Advanced Materials programme and was supported by MCIN with funding from European Union NextGenerationEU (PRTR-C17.I1) and by Generalitat de Catalunya (In-CAEM Project). The authors thank support from the project AMaDE (PID2023-149158OB-C43), funded by MCIN/ AEI/ 10.13039/501100011033/ and by "ERDF A way of making Europe", by the "European Union". ICN2 is supported by the Severo Ochoa program from Spanish MCIN / AEI (Grant No.: CEX2021-001214-S). ICN2 and IREC are funded by the CERCA Programme / Generalitat de Catalunya. ICN2 is the founding member of e-DREAM (https://doi.org/10.1017/S1431927622010893). X.H. and T.Z. acknowledge support from Marie Skłodowska-Curie grant agreement number 101146498 and 101105092. W. T. acknowledges for the financial support from the National Natural Science Foundation of China (Grant No. 22108070) and the Young Elite Scientists Sponsorship Program by CAST (No. 2022QNRC001). KD acknowledges support from the Novo Nordisk Foundation CO_2 Research Center (Grant no. NNF21SA0072700); this work is published under the number CORC_25_47.

Appendix A. Supplementary data

Supplementary data to this article can be found online at https://doi.org/10.1016/j.cej.2025.160634.

Data availability

Data will be made available on request.

References

[1] P. Papangelakis, R.K. Miao, R. Lu, H. Liu, X. Wang, A. Ozden, S. Liu, N. Sun, C. P. O'Brien, Y. Hu, M. Shakouri, Q. Xiao, M. Li, B. Khatir, J.E. Huang, Y. Wang, Y. C. Xiao, F. Li, A.S. Zeraati, Q. Zhang, P. Liu, K. Golovin, J.Y. Howe, H. Liang, Z. Wang, J. Li, E.H. Sargent, D. Sinton, Improving the SO_2 tolerance of CO_2 reduction electrocatalysts using a polymer/catalyst/ionomer heterojunction design, Nat. Energy 9 (8) (2024) 1011–1020, https://doi.org/10.1038/s41560-024-01577-9.

[2] J. Yu, J. Xiao, L. Guo, Z. Xie, K. Wang, Y. Wang, F. Hao, Y. Ma, J. Zhou, P. Lu, G. Wang, X. Meng, Z. Zhu, Q. Li, C. Ling, J. Sun, Y. Wang, S. Song, Z. Fan, In situ phase transformation-enabled metal–organic frameworks for efficient CO_2 electroreduction to multicarbon products in strong acidic media, ACS Nano (2024), https://doi.org/10.1021/acsnano.4c12245.

[3] Š. Kment, A. Bakandritsos, I. Tantis, H. Kmentová, Y. Zuo, O. Henrotte, A. Naldoni, M. Otyepka, R.S. Varma, R. Zboril, Single atom catalysts based on earth-abundant metals for energy-related applications, Chem. Rev. 124 (21) (2024) 11767–11847, https://doi.org/10.1021/acs.chemrev.4c00155.

[4] M. Li, H. Wang, W. Luo, P.C. Sherrell, J. Chen, J. Yang, Heterogeneous single-atom catalysts for electrochemical CO_2 reduction reaction, Adv. Mater. 32 (34) (2020) 2001848, https://doi.org/10.1002/adma.202001848.

[5] Y. Wang, Y. Liu, W. Liu, J. Wu, Q. Li, Q. Feng, Z. Chen, X. Xiong, D. Wang, Y. Lei, Regulating the coordination structure of metal single atoms for efficient electrocatalytic CO_2 reduction, Energy Environ. Sci. 13 (12) (2020) 4609–4624, https://doi.org/10.1039/D0EE02833A.

[6] Q. Qu, S. Ji, Y. Chen, D. Wang, Y. Li, The atomic-level regulation of single-atom site catalysts for the electrochemical CO_2 reduction reaction, Chem. Sci. 12 (12) (2021) 4201–4215, https://doi.org/10.1039/D0SC07040H.

[7] L. Kong, M. Wang, L. Jiang, Heteroatom-doped asymmetric metal-Nx-C single atom catalysts for electrochemical CO_2 reduction reaction, Chem. Asian J. 17 (24) (2022) e202200939, https://doi.org/10.1002/asia.202200939.

[8] S. Wang, L. Wang, D. Wang, Y. Li, Recent advances of single-atom catalysts in CO_2 conversion, Energy Environ. Sci. 16 (7) (2023) 2759–2803, https://doi.org/10.1039/D3EE00037K.

[9] D. Zhao, K. Yu, P. Song, W. Feng, B. Hu, W.-C. Cheong, Z. Zhuang, S. Liu, K. Sun, J. Zhang, C. Chen, Atomic-level engineering $Fe_1N_2O_2$ interfacial structure derived from oxygen-abundant metal–organic frameworks to promote electrochemical CO_2 reduction, Energy Environ. Sci. 15 (9) (2022) 3795–3804, https://doi.org/10.1039/D2EE00878E.

[10] Y. Li, Y. Ding, B. Zhang, Y. Huang, H. Qi, P. Das, L. Zhang, X. Wang, Z.-S. Wu, X. Bao, N,O symmetric double coordination of an unsaturated Fe single-atom confined within a graphene framework for extraordinarily boosting oxygen reduction in Zn–air batteries, Energy Environ. Sci. 16 (6) (2023) 2629–2636, https://doi.org/10.1039/D3EE00747B.

[11] Z. Chen, C. Wang, X. Zhong, H. Lei, J. Li, Y. Ji, C. Liu, M. Ding, Y. Dai, X. Li, T. Zheng, Q. Jiang, H.-J. Peng, C. Xia, Achieving efficient CO_2 electrolysis to CO by local coordination manipulation of nickel single-atom catalysts, Nano Lett. 23 (15) (2023) 7046–7053, https://doi.org/10.1021/acs.nanolett.3c01808.

[12] Y. Li, Y. Ji, Y. Zhao, J. Chen, S. Zheng, X. Sang, B. Yang, Z. Li, L. Lei, Z. Wen, X. Feng, Y. Hou, Local spin-state tuning of iron single-atom electrocatalyst by S-coordinated doping for kinetics-boosted ammonia synthesis, Adv. Mater. 34 (28) (2022) 2202240, https://doi.org/10.1002/adma.202202240.

[13] M. Qu, Z. Chen, Z. Sun, D. Zhou, W. Xu, H. Tang, H. Gu, T. Liang, P. Hu, G. Li, Y. Wang, Z. Chen, T. Wang, B. Jia, Rational design of asymmetric atomic Ni-P_1N_3 active sites for promoting electrochemical CO_2 reduction, Nano Res. 16 (2) (2023) 2170–2176, https://doi.org/10.1007/s12274-022-4969-z.

[14] K. Li, S. Zhang, X. Zhang, S. Liu, H. Jiang, T. Jiang, C. Shen, Y. Yu, W. Chen, Atomic tuning of single-atom Fe–N–C catalysts with phosphorus for robust electrochemical CO_2 reduction, Nano Lett. 22 (4) (2022) 1557–1565, https://doi.org/10.1021/acs.nanolett.1c04382.

[15] W. Yan, W. Chen, Y. Chen, Recent design strategies for M-N-C single-atom catalysts in oxygen reduction: an entropy increase perspective, Adv. Funct. Mater. 34 (36) (2024) 2401027, https://doi.org/10.1002/adfm.202401027.

[16] J. Huang, S. Yang, S. Jiang, C. Sun, S. Song, Entropy-increasing single-atom photocatalysts strengthening the polarization field for boosting H_2O overall splitting into H_2, ACS Catal. 12 (23) (2022) 14708–14716, https://doi.org/10.1021/acscatal.2c05014.

[17] W. Ni, H. Chen, J. Zeng, Y. Zhang, H.A. Younus, Z. Zeng, M. Dai, W. Zhang, S. Zhang, Regulating nonmetallic species beyond the first coordination shell of single-atom catalysts for high-performance electrocatalysis, Energy Environ. Sci. 16 (9) (2023) 3679–3710, https://doi.org/10.1039/D3EE02090H.

[18] S. Chen, X. Li, C.-W. Kao, T. Luo, K. Chen, J. Fu, C. Ma, H. Li, M. Li, T.-S. Chan, M. Liu, Unveiling the proton-feeding effect in sulfur-doped Fe−N−C single-atom catalyst for enhanced CO_2 electroreduction, Angew. Chem. Int. Ed. 61 (32) (2022) e202206233, https://doi.org/10.1002/anie.202206233.

[19] C. Jia, X. Tan, Y. Zhao, W. Ren, Y. Li, Z. Su, S.C. Smith, C. Zhao, Sulfur-dopant-promoted electroreduction of CO_2 over coordinatively unsaturated Ni-N_2 moieties, Angew. Chem. Int. Ed. 60 (43) (2021) 23342–23348, https://doi.org/10.1002/anie.202109373.

[20] Y. Wang, P. Zhu, R. Wang, K.C. Matthews, M. Xie, M. Wang, C. Qiu, Y. Liu, H. Zhou, J.H. Warner, Y. Liu, H. Wang, G. Yu, Fluorine-tuned carbon-based nickel single-atom catalysts for scalable and highly efficient CO_2 electrocatalytic reduction, ACS Nano 18 (39) (2024) 26751–26758, https://doi.org/10.1021/acsnano.4c06923.

[21] Q.-Q. Tang, L.-F. Feng, Z.-P. Li, S.-H. Wu, L.-S. Zhang, Q. Sun, M.-F. Wu, J.-P. Zou, Single-atom sites regulation by the second-shell doping for efficient electrochemical CO_2 reduction, Chin. Chem. Lett. 35 (9) (2024) 109454, https://doi.org/10.1016/j.cclet.2023.109454.

[22] Q. Wang, K. Liu, K. Hu, C. Cai, H. Li, H. Li, M. Herran, Y.-R. Lu, T.-S. Chan, C. Ma, J. Fu, S. Zhang, Y. Liang, E. Cortés, M. Liu, Attenuating metal-substrate conjugation in atomically dispersed nickel catalysts for electroreduction of CO_2 to CO, Nat. Commun. 13 (1) (2022) 6082, https://doi.org/10.1038/s41467-022-33692-0.

[23] T. Zhang, X. Han, H. Liu, M. Biset-Peiró, X. Zhang, P. Tan, P. Tang, B. Yang, L. Zheng, J.R. Morante, J. Arbiol, Quasi-double-star nickel and iron active sites for high-efficiency carbon dioxide electroreduction, Energy Environ. Sci. 14 (9) (2021) 4847–4857, https://doi.org/10.1039/D1EE01592C.

[24] C. Xiao, L. Cheng, Y. Zhu, G. Wang, L. Chen, Y. Wang, R. Chen, Y. Li, C. Li, Super-coordinated nickel $N_4Ni_1O_2$ site single-atom catalyst for selective H_2O_2 electrosynthesis at high current densities, Angew. Chem. Int. Ed. 61 (38) (2022) e202206544, https://doi.org/10.1002/anie.202206544.

[25] T. Zhang, X. Han, H. Liu, M. Biset-Peiró, J. Li, X. Zhang, P. Tang, B. Yang, L. Zheng, J.R. Morante, J. Arbiol, Site-specific axial oxygen coordinated FeN_4 active sites for highly selective electroreduction of carbon dioxide, Adv. Funct. Mater. 32 (18) (2022) 2111446, https://doi.org/10.1002/adfm.202111446.

[26] Z. Jin, D. Jiao, Y. Dong, L. Liu, J. Fan, M. Gong, X. Ma, Y. Wang, W. Zhang, L. Zhang, Z. Gen Yu, D. Voiry, W. Zheng, X. Cui, Boosting electrocatalytic carbon dioxide reduction via self-relaxation of asymmetric coordination in Fe-based single atom catalyst, Angew. Chem. Int. Ed. 63 (6) (2024) e202318246, https://doi.org/10.1002/anie.202318246.

[27] L. Ye, Y. Ying, D. Sun, Z. Zhang, L. Fei, Z. Wen, J. Qiao, H. Huang, Highly efficient porous carbon electrocatalyst with controllable N-species content for selective CO_2 reduction, Angew. Chem. Int. Ed. 59 (8) (2020) 3244–3251, https://doi.org/10.1002/anie.201912751.

[28] X. Lv, Y. Tian, F. Wu, X. Luan, F. Li, Z. Shen, G. Xu, K. Liu, W. Niu, Chiral plasmonic-dielectric coupling enables strong near-infrared chiroptical responses from helicoidal core-shell nanoparticles, Nat. Commun. 15 (1) (2024) 9234, https://doi.org/10.1038/s41467-024-53705-4.

[29] S. Ding, J.A. Barr, Z. Lyu, F. Zhang, M. Wang, P. Tieu, X. Li, M.H. Engelhard, Z. Feng, S.P. Beckman, X. Pan, J.-C. Li, D. Du, Y. Lin, Effect of phosphorus

modulation in iron single-atom catalysts for peroxidase mimicking, Adv. Mater. 36 (10) (2024) 2209633, https://doi.org/10.1002/adma.202209633.
[30] J. Li, G. Wang, X. Wang, Y. Zhao, Y. Zhao, W. Sui, D. Wang, C. Si, Oriented conversion of HMF to FDCA under mild conditions over lignin-tailored Co single-atom catalyst with enhanced co loadings, ACS Catal. 14 (21) (2024) 16003–16013, https://doi.org/10.1021/acscatal.4c04419.
[31] W. Zhang, H. Li, D. Feng, C. Wu, C. Sun, B. Jia, X. Liu, T. Ma, MOF-derived 1D/3D N-doped porous carbon for spatially confined electrochemical CO_2 reduction to adjustable syngas, Carbon Energy 6 (8) (2024) e461.
[32] C. Hu, S. Bai, L. Gao, S. Liang, J. Yang, S.-D. Cheng, S.-B. Mi, J. Qiu, Porosity-induced high selectivity for CO_2 electroreduction to CO on Fe-doped ZIF-derived carbon catalysts, ACS Catal. 9 (12) (2019) 11579–11588, https://doi.org/10.1021/acscatal.9b03175.
[33] Y.-M. Wang, F.-Q. Yan, Q.-Y. Wang, C.-X. Du, L.-Y. Wang, B. Li, S. Wang, S.-Q. Zang, Single-atom tailored atomically-precise nanoclusters for enhanced electrochemical reduction of CO_2-to-CO activity, Nat. Commun. 15 (1) (2024) 1843, https://doi.org/10.1038/s41467-024-46098-x.
[34] X. Li, S.-G. Han, W. Wu, K. Zhang, B. Chen, S.-H. Zhou, D.-D. Ma, W. Wei, X.-T. Wu, R. Zou, Q.-L. Zhu, Convergent paired electrosynthesis of dimethyl carbonate from carbon dioxide enabled by designing the superstructure of axial oxygen coordinated nickel single-atom catalysts, Energy Environ. Sci. 16 (2) (2023) 502–512, https://doi.org/10.1039/D2EE03022E.
[35] M. Wen, N. Sun, L. Jiao, S.-Q. Zang, H.-L. Jiang, Microwave-assisted rapid synthesis of MOF-based single-atom Ni catalyst for CO_2 electroreduction at ampere-level current, Angew. Chem. Int. Ed. 63 (10) (2024) e202318338, https://doi.org/10.1002/anie.202318338.
[36] A. Martini, D. Hursán, J. Timoshenko, M. Rüscher, F. Haase, C. Rettenmaier, E. Ortega, A. Etxebarria, B. Roldan Cuenya, Tracking the evolution of single-atom catalysts for the CO_2 electrocatalytic reduction using operando X-ray absorption spectroscopy and machine learning, J. Am. Chem. Soc. 145(31) (2023) 17351-17366. 10.1021/jacs.3c04826.
[37] R. Li, Z. Zhang, X. Liang, J. Shen, J. Wang, W. Sun, D. Wang, J. Jiang, Y. Li, Polystyrene waste thermochemical hydrogenation to ethylbenzene by a N-bridged Co, Ni dual-atom catalyst, J Am. Chem. Soc. 145 (29) (2023) 16218–16227, https://doi.org/10.1021/jacs.3c05184.
[38] Y.E. Kim, Y.N. Ko, B.-S. An, J. Hong, Y.E. Jeon, H.J. Kim, S. Lee, J. Lee, W. Lee, Atomically dispersed nickel coordinated with nitrogen on carbon nanotubes to boost electrochemical CO_2 reduction, ACS Energy Lett. 8 (8) (2023) 3288–3296, https://doi.org/10.1021/acsenergylett.3c00933.
[39] M. Huang, B. Deng, X. Zhao, Z. Zhang, F. Li, K. Li, Z. Cui, L. Kong, J. Lu, F. Dong, L. Zhang, P. Chen, Template-sacrificing synthesis of well-defined asymmetrically coordinated single-atom catalysts for highly efficient CO_2 electrocatalytic reduction, ACS Nano 16 (2) (2022) 2110–2119, https://doi.org/10.1021/acsnano.1c07746.
[40] X. Wang, Y. Wang, X. Sang, W. Zheng, S. Zhang, L. Shuai, B. Yang, Z. Li, J. Chen, L. Lei, N.M. Adli, M.K.H. Leung, M. Qiu, G. Wu, Y. Hou, Dynamic activation of adsorbed intermediates via axial traction for the promoted electrochemical CO_2 reduction, Angew. Chem. Int. Ed. 60 (8) (2021) 4192–4198, https://doi.org/10.1002/anie.202013427.
[41] J. Chen, H. Li, C. Fan, Q. Meng, Y. Tang, X. Qiu, G. Fu, T. Ma, Dual single-atomic Ni-N_4 and Fe-N_4 sites constructing janus hollow graphene for selective oxygen electrocatalysis, Adv. Mater. 32 (30) (2020) 2003134, https://doi.org/10.1002/adma.202003134.
[42] Y.-N. Gong, L. Jiao, Y. Qian, C.-Y. Pan, L. Zheng, X. Cai, B. Liu, S.-H. Yu, H.-L. Jiang, Regulating the coordination environment of MOF-templated single-atom nickel electrocatalysts for boosting CO_2 reduction, Angew. Chem. Int. Ed. 59 (7) (2020) 2705–2709, https://doi.org/10.1002/anie.201914977.
[43] J. Zhang, Y. Zhao, C. Chen, Y.-C. Huang, C.-L. Dong, C.-J. Chen, R.-S. Liu, C. Wang, K. Yan, Y. Li, G. Wang, Tuning the coordination environment in single-atom catalysts to achieve highly efficient oxygen reduction reactions, J. Am. Chem. Soc. 141 (51) (2019) 20118–20126, https://doi.org/10.1021/jacs.9b09352.
[44] H. Li, K. Gan, R. Li, H. Huang, J. Niu, Z. Chen, J. Zhou, Y. Yu, J. Qiu, X. He, Highly dispersed NiO clusters induced electron delocalization of Ni-N-C catalysts for enhanced CO_2 electroreduction, Adv. Funct. Mater. 33 (1) (2023) 2208622, https://doi.org/10.1002/adfm.202208622.
[45] X. Han, T. Zhang, M. Biset-Peiró, X. Zhang, J. Li, W. Tang, P. Tang, J.R. Morante, J. Arbiol, Engineering the interfacial microenvironment via surface hydroxylation to realize the global optimization of electrochemical CO_2 reduction, ACS Appl. Mater. Interfaces 14 (28) (2022) 32157–32165, https://doi.org/10.1021/acsami.2c09129.
[46] X. Han, T. Zhang, M. Biset-Peiró, S. Zhao, S. Murcia Lopez, K. Daasbjerg, J. R. Morante, J. Li, J. Arbiol, A MOF-based spatial-separation layer to enable a uniform favorable microenvironment for electrochemical CO_2 reduction, Small Struct. 4 (8) (2023) 2200388, https://doi.org/10.1002/sstr.202200388.
[47] M. Huang, S.-H. Zhou, C.-J. Yang, C.-L. Dong, Y. He, W. Wei, X. Li, Q.-L. Zhu, Z. Huang, Selenic acid etching assisted atomic engineering for designing metal-semimetal dual single-atom catalysts for enhanced CO_2 electroreduction, ACS Nano 18 (48) (2024) 33210–33219, https://doi.org/10.1021/acsnano.4c12576.
[48] W. Ren, X. Tan, W. Yang, C. Jia, S. Xu, K. Wang, S.C. Smith, C. Zhao, Isolated diatomic Ni-Fe metal–nitrogen sites for synergistic electroreduction of CO_2, Angew. Chem. Int. Ed. 58 (21) (2019) 6972–6976, https://doi.org/10.1002/anie.201901575.
[49] C. Zhao, Y. Wang, Z. Li, W. Chen, Q. Xu, D. He, D. Xi, Q. Zhang, T. Yuan, Y. Qu, J. Yang, F. Zhou, Z. Yang, X. Wang, J. Wang, J. Luo, Y. Li, H. Duan, Y. Wu, Y. Li, Solid-diffusion synthesis of single-atom catalysts directly from bulk metal for efficient CO_2 reduction, Joule 3 (2) (2019) 584–594, https://doi.org/10.1016/j.joule.2018.11.008.
[50] X. Qin, S. Zhu, F. Xiao, L. Zhang, M. Shao, Active sites on heterogeneous single-iron-atom electrocatalysts in CO_2 reduction reaction, ACS Energy Lett. 4 (7) (2019) 1778–1783, https://doi.org/10.1021/acsenergylett.9b01015.
[51] X. Ren, J. Zhao, X. Li, J. Shao, B. Pan, A. Salamé, E. Boutin, T. Groizard, S. Wang, J. Ding, X. Zhang, W.-Y. Huang, W.-J. Zeng, C. Liu, Y. Li, S.-F. Hung, Y. Huang, M. Robert, B. Liu, In-situ spectroscopic probe of the intrinsic structure feature of single-atom center in electrochemical CO/CO_2 reduction to methanol, Na. Commun. 14 (1) (2023) 3401, https://doi.org/10.1038/s41467-023-39153-6.
[52] J. Chen, T. Wang, X. Wang, B. Yang, X. Sang, S. Zheng, S. Yao, Z. Li, Q. Zhang, L. Lei, J. Xu, L. Dai, Y. Hou, Promoting electrochemical CO_2 reduction via boosting activation of adsorbed intermediates on iron single-atom catalyst, Adv. Funct. Mater. 32 (21) (2022) 2110174, https://doi.org/10.1002/adfm.202110174.
[53] W. Zhu, L. Zhang, S. Liu, A. Li, X. Yuan, C. Hu, G. Zhang, W. Deng, K. Zang, J. Luo, Y. Zhu, M. Gu, Z.-J. Zhao, J. Gong, Enhanced CO_2 electroreduction on neighboring Zn/Co monomers by electronic effect, Angew. Chem. Int. Ed. 59 (31) (2020) 12664–12668, https://doi.org/10.1002/anie.201916218.
[54] Y. Yang, J. Li, C. Zhang, Z. Yang, P. Sun, S. Liu, Q. Cao, Theoretical insights into nitrogen-doped graphene-supported Fe, Co, and Ni as single-atom catalysts for CO_2 reduction reaction, J. Phys. Chem. C 126 (9) (2022) 4338–4346, https://doi.org/10.1021/acs.jpcc.1c09740.